Research in Astronomy and Astrophysics, 22:105017 (9pp), 2022 October https://doi.org/10.1088/1674-4527/ac8f8a

Investigation of the Oscillations in a Flare-productive Active Region

Fanpeng Shi[1,2], Zongjun Ning[1,2], and Dong Li[1,2]

[1] Key Laboratory of Dark Matter and Space Science, Purple Mountain Observatory, Chinese Academy of Sciences, Nanjing 210033, China; shifp@pmo.ac.cn

[2] School of Astronomy and Space Science, University of Science and Technology of China, Hefei 230026, China

Received 2022 July 15; revised 2022 August 17; accepted 2022 August 31; published 2022 October 4

Abstract

We investigate the oscillations in active region (AR) NOAA 12891, which produces a C2.0 three-ribbon flare accompanying a jet on 2021 November 2. Using the data from the Atmospheric Imaging Assembly onboard the Solar Dynamics Observatory, the 5 minutes decayless kink oscillations of coronal loops were detected and they are independent of the solar flare. Based on the observed oscillations and seismological diagnostics, we estimate that the Alfvén speed and magnetic field in these coronal loops are around 466 km s^{-1} and 7.6 G, respectively. Additionally, the flare-related jet shows its plasmoids with 1 minute periodicity same as the intensity fluctuation of nearby flare ribbon. The correlation between the intensity fluctuation of jet and that of flare ribbon indicates that their 1 minute oscillations should originate from the same reconnection process.

Key words: Sun: activity – Sun: oscillations – Sun: UV radiation

Online material: animation

1. Introduction

Oscillation is the prevalent phenomenon in the Sun. It is common that oscillations exist in the various objects of the active region (AR), such as coronal loops (Nakariakov & Kolotkov 2020), flares (Zimovets et al. 2021), jets, and filaments (or prominences) (Arregui et al. 2018).

The kink oscillation is the periodic transverse displacements of coronal loops, which was interpreted as the standing fast kink waves (Nakariakov et al. 2021). Kink oscillations can be divided into two main types, such as decaying (Aschwanden et al. 1999; Nakariakov et al. 1999; Schrijver et al. 2002; White & Verwichte 2012) and decayless (Tian et al. 2012; Nisticò et al. 2013; Anfinogentov et al. 2015; Gao et al. 2022) cases. The decaying kink oscillations are usually triggered by nearby eruptions (Zimovets & Nakariakov 2015), and they will experience rapidly damping during their lifetimes. In the decayless cases, coronal loops can last for several cycles without significant damping, while its excitation mechanism is still an open issue, e.g., a harmonic driver (Nisticò et al. 2013), a self-oscillation model (Nakariakov et al. 2016), a random driver (Afanasyev et al. 2020), etc.

The flare oscillations generally refer to the quasi-periodic pulsations (QPPs), which are the periodic behavior of flare light curves. QPPs can occur in all bands of electromagnetic waves, and usually with multiple periods. Their characteristic periods range from subseconds to several minutes. The reasons of QPPs are usually explained as the magnetohydrodynamic (MHD) oscillations in coronal magnetic loops or quasi-periodic magnetic reconnection (Nakariakov & Melnikov 2009; Van Doorsselaere et al. 2016; McLaughlin et al. 2018; Kupriyanova et al. 2020; Zimovets et al. 2021). However, it is not yet possible to get a definite conclusion of its origin due to the lack of sufficient observational information. Furthermore, the characteristic periods of QPPs are similar to quasi-periodic fast-propagating (QFP) magnetosonic wave trains, and they might be two different aspects of the same physical process (e.g., Liu et al. 2011; Shen & Liu 2012; Shen et al. 2018a, 2018b, 2022; Miao et al. 2021).

The jet refers to the ejection of outward plasmoids (plasma blobs). Based on previous observations, it was found that successive plasmoids ejection in the jet (Zhang & Ji 2014; Shen et al. 2017, 2019a; Zhang & Ni 2019), which is the typical indication for magnetic reconnection due to the tearing-mode instability of the current sheets (Shen 2021). Therefore, the periodic plasmoids in the jet manifest the characteristic period of reconnection. Hong et al. (2022) reported a long-duration jet in which 5 minutes intensity oscillation originated from continuous magnetic reconnection modulated by p-modes oscillations.

According to the velocity amplitudes, filament oscillations are usually classified as large-amplitude and small-amplitude oscillations (Oliver & Ballester 2002). In general, large-amplitude oscillations are triggered by external disturbances, such as Moreton waves, extreme ultraviolet (EUV) waves, shock waves, flares, and jets (e.g., Okamoto et al. 2004; Asai et al. 2012; Liu et al. 2013; Luna et al. 2014; Shen et al. 2014a, 2014b; Zhang & Ji 2018). Small-amplitude oscillations in filaments are local in nature and thread perturbations had been observed (Lin et al. 2007; Okamoto et al. 2007; Ning et al. 2009; Li et al. 2018, 2022).

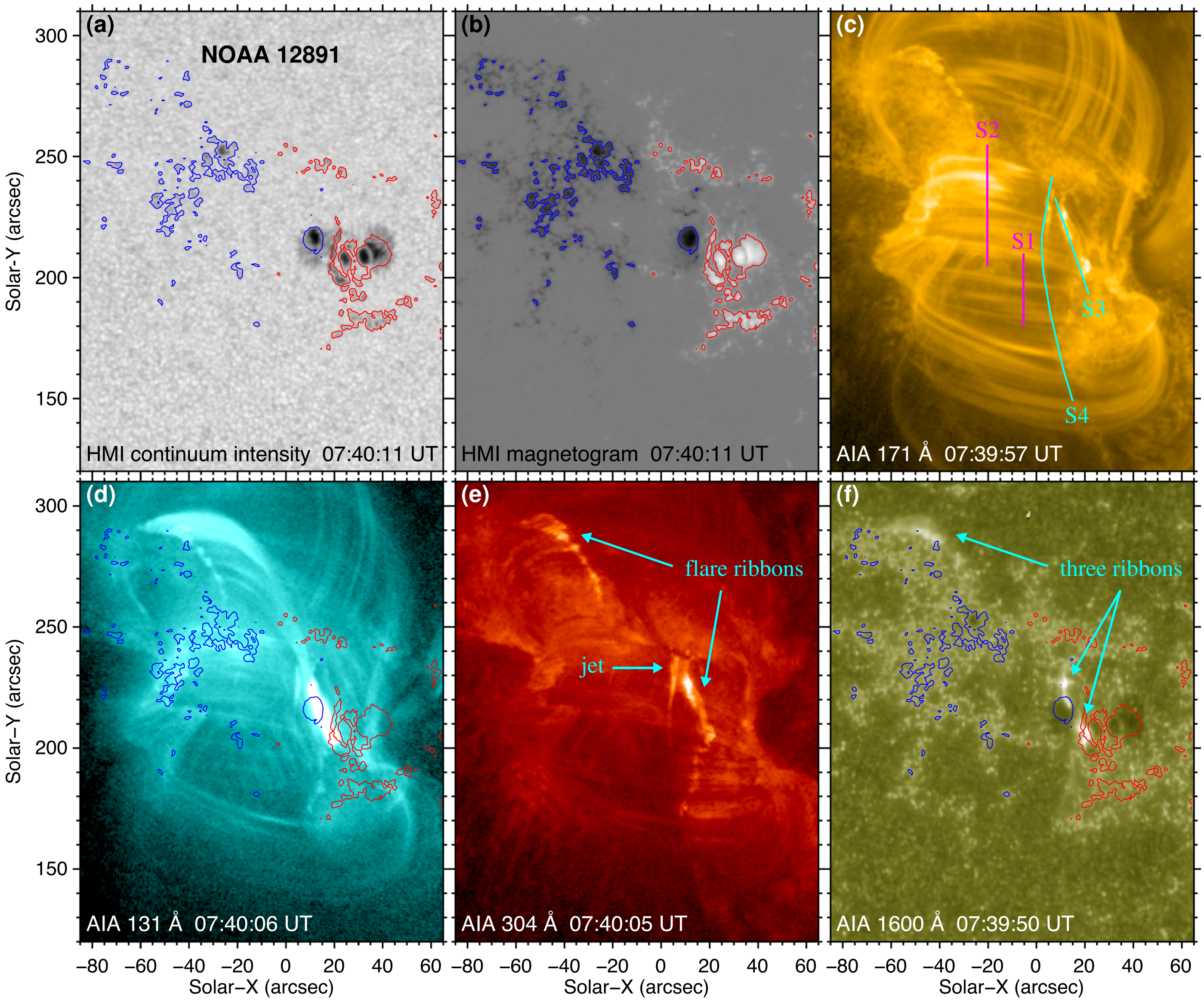

Figure 1. (a), (b) SDO/HMI continuum intensity image and LOS magnetogram of AR 12891. Red and blue contours represent 500 and –500 G, respectively. (c)–(f) Flare images observed by SDO/AIA in 171, 131, 304, and 1600 Å.

(An animation of this figure is available.)

In this paper, we investigate the oscillations in a flare-productive AR, including the decayless kink oscillations of coronal loops, and the intensity oscillations of flare ribbon and of flare-related jet. This AR was observed by the Atmospheric Imaging Assembly (AIA; Lemen et al. 2012), and the Helioseismic and Magnetic Imager (HMI; Schou et al. 2012) onboard the Solar Dynamics Observatory (SDO; Pesnell et al. 2012). All of the above data have been removed solar rotation by derotating to 08:00 UT. In Section 2, we describe the observations of the AR, which are followed by the data analysis in Section 3. The discussion and conclusions are provided in Section 4.

2. Observations

The AR studied here is NOAA 12891 during the period from 07:20 UT to 08:30 UT on 2021 November 2. It is located at N17W00, almost near the solar disk center. It has about 150″ width along east–west direction and about 200″ length along north–south direction. According to the categorization of sunspots (Toriumi & Wang 2019), the magnetic configuration of this AR is classified as β type at the photospheric level, as shown in Figures 1(a) and (b), which present the HMI continuum intensity image and the line-of-sight (LOS)

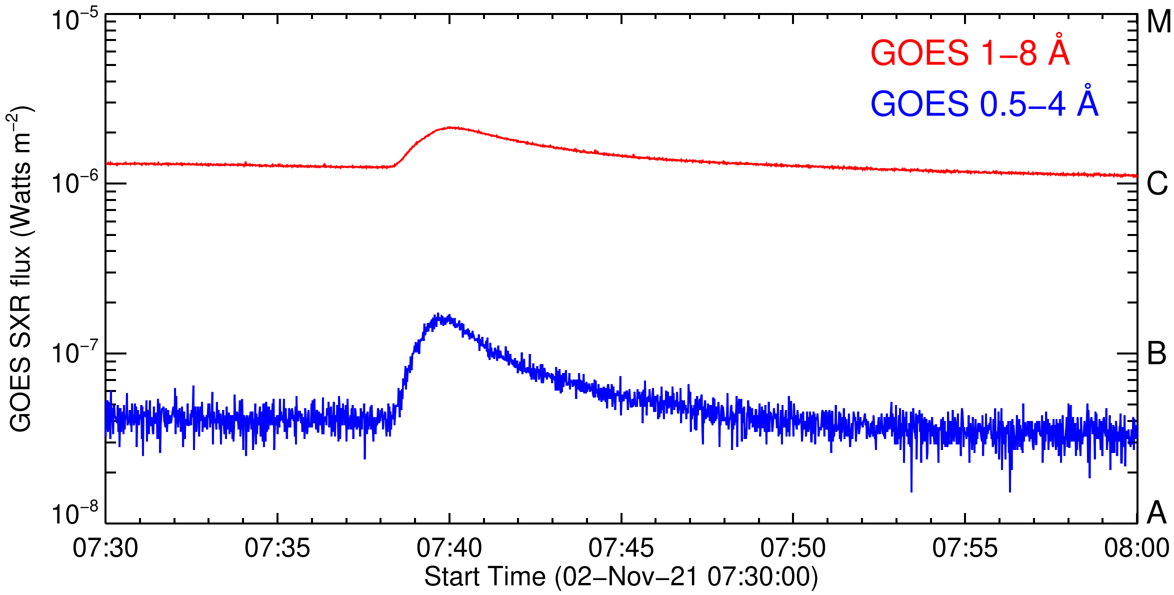

Figure 2. The *GOES* soft X-ray flux between 07:30 UT and 08:00 UT.

magnetogram. The maximum values of positive and negative fields are about 1600 G and −1500 G, respectively. Red and blue contours represent ±500 G in Figure 1. The preceding spots and the following spots show the positive and negative polarities, as usual as magnetic field configuration on the northern hemisphere during the odd solar activity cycles (2021 belongs to the 25th solar cycle). The preceding spots are closer to the equator. Meanwhile, there are lots of magnetic poles composed into the preceding and following spots. Such complicated configuration of photospheric fields results into the coronal loops interlacing each other, as AIA 171 Å image in Figure 1(c), which shows the side observations of large-scale loop systems located at the northern and southern of this AR. From AIA 171 Å animation between 07:20 UT and 08:30 UT (AIA_171.mp4), we find these coronal loops are almost stable, although some bright structures propagating along them. However, the coronal loops in the middle of AR, location between 180″ and 250″ along Solar-*Y*-axis, are oscillating with time.

In addition, there is a solar flare eruption in this AR. It was a C2.0 class event, and started at 07:37 UT, peaked at 07:40 UT and ended at 07:44 UT according to Geostationary Operational Environmental Satellite (*GOES*) soft X-ray (SXR) flux, as shown in Figure 2.

This event is well detected by SDO/AIA. EUV emission of AIA 131 Å channel for flaring corona comes primarily from Fe XXI 128.75 Å line ($T \sim 1.1 \times 10^7$ K). AIA 171 Å is expected to observe the Fe IX 171.07 Å line ($T \sim 7 \times 10^5$ K) for the upper transition region/quiet corona (O'Dwyer et al. 2010). The 304 Å channel is dominated by the two He II 303.8 Å lines ($T \sim 5 \times 10^4$ K), which is expected to detect the chromosphere/transition region. Based on C IV lines (near 1600 Å, $T \sim 10^5$ K) and nearby continuum ($T \sim 5 \times 10^3$ K), AIA 1600 Å has a broad response from the upper photosphere to transition region, but the UV continuum of the upper photosphere dominates this channel.

Figures 1(c)–(f) show AIA 171, 131, 304, and 1600 Å images at 07:40 UT near the flare maximum phase. There are two ribbons on AIA 304 Å image, and flare loops connected them on AIA 131 Å image. However, as what can be seen in the 1600 Å image, the south ribbon could be a double-ribbon flare itself, thus the eruption could be a three-ribbon flare, as there were marked in Figure 1(f), the northeast, middle and southwest ribbon, and this is consistent with eruptions within a fan-spine topology (Masson et al. 2009; Pariat et al. 2010; Wang & Liu 2012; Shen et al. 2019b). The brightening of two south ribbons preceded the northeast ribbon, and the latter can be regarded as the remote brightening in the fan-spine reconnection eruption. Moreover, it is interesting that the jet intermittent erupted into the corona from the flare ribbon during the flaring time, and the jet showed an obvious twisting structure (07:40 UT) as what had been observed by Shen et al. (2011). The jet could be generated through the reconnection between the newly formed post-flare-loop in the fan-spine reconnection and the pre-existing ambient loop rooted in the positive polarity region next to the minor negative polarity located at the north of the compact negative polarity. There is a small loop structure at the west of the jet-base, which is the supporting evidence for the occurrence of the jet.

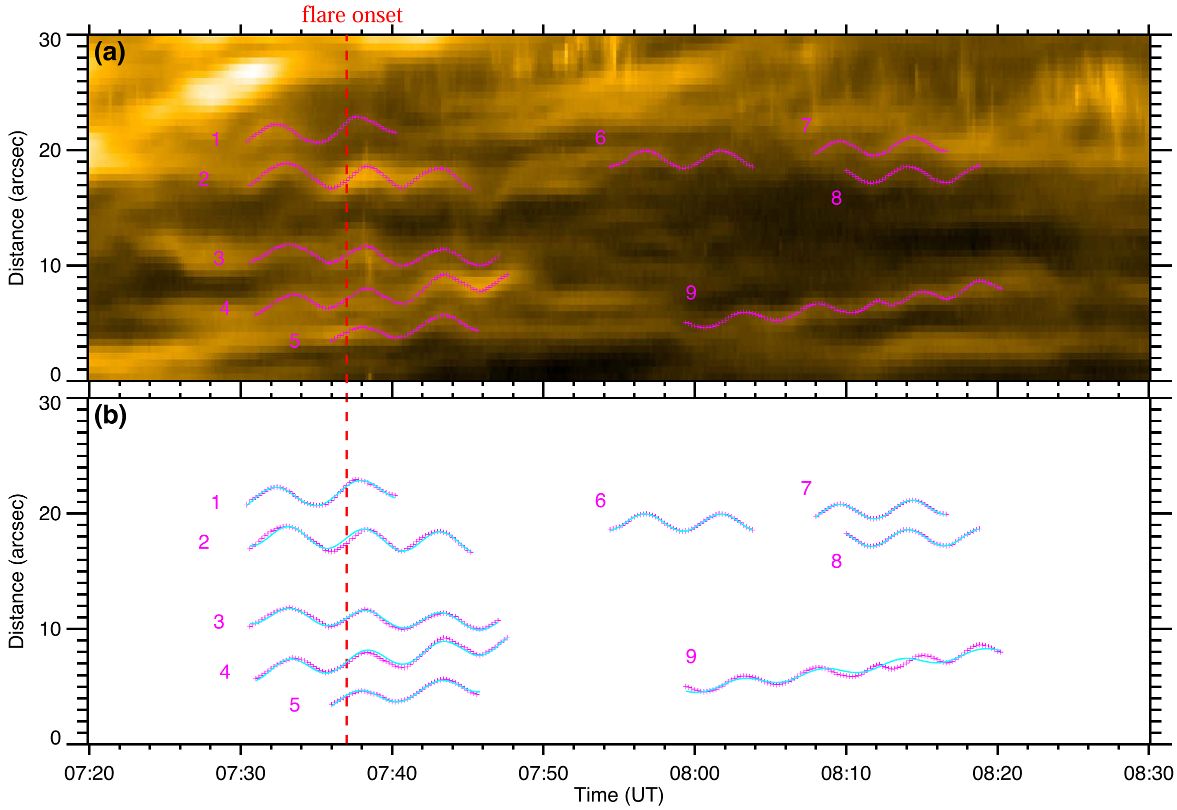

Figure 3. (a) Time–distance diagram of slit-1 in Figure 1(c), and the vertical red dotted line labels the onset of flare. The magenta pluses represent the points we manually select along the bright pixels. (b) Cyan curves draw sinusoidal fits of oscillating coronal loops, and their key parameters are listed in Table 1.

Table 1
Key Parameters of Oscillations in Figure 3

Parameter	1	2	3	4	5	6	7	8	9
Oscillatory period, P (min)	5.64	5.01	5.00	5.06	5.39	5.03	4.80	4.80	5.29
Displacement amplitude, A_m (Mm)	0.71	0.67	0.53	0.59	0.53	0.55	0.53	0.53	0.28
Radius of the loop cross-section, R (Mm)	0.86	0.82	0.74	0.62	0.75	0.69	0.61	⋯	0.66

3. Data Analysis

3.1. Oscillations in Coronal Loops

As mentioned before, the oscillating loops are located in the middle of AR. To show the oscillations in detail, we outline two artificial slits (slit-1 and 2) in Figure 1(c) as the cyan and magenta vertical lines. Slit-1 have a full width of 3″ (5 pixels) and slit-2 is 12″ (20 pixels). Slit-1 is located at the position of inclined coronal loops, while slit-2 is on the top of loops, which result in the oscillatory behavior with different pictures. In other words, when the loops display the transverse oscillations, we can detect the transverse wave from the loop side view, like as slit-1, while maybe only the dark or bright structure from the loop top (when loops displace along LOS), like as slit-2. Figure 3(a) plots the time–distance diagram of loop oscillation from 07:20 UT to 08:30 UT. The Y-axis is from solar south to north. Same as our imagine, there are many transverse oscillating structures. Based on the local maximum brightness marked by magenta pluses, in total nine trajectories are outlined. Then, we use a sinusoidal function with a linear background to fit these trajectories. The fitting function (Zhang et al. 2020; Dai et al. 2021; Li et al. 2022) is

$$A(t) = A_m \sin\left(\frac{2\pi}{P}t + \phi\right) + kt + A_0, \quad (1)$$

where A_m represents the displacement amplitude, P is the oscillatory period, ϕ is the initial phase, and $kt + A_0$ is a linear term of the equilibrium position, in which k is the drifting

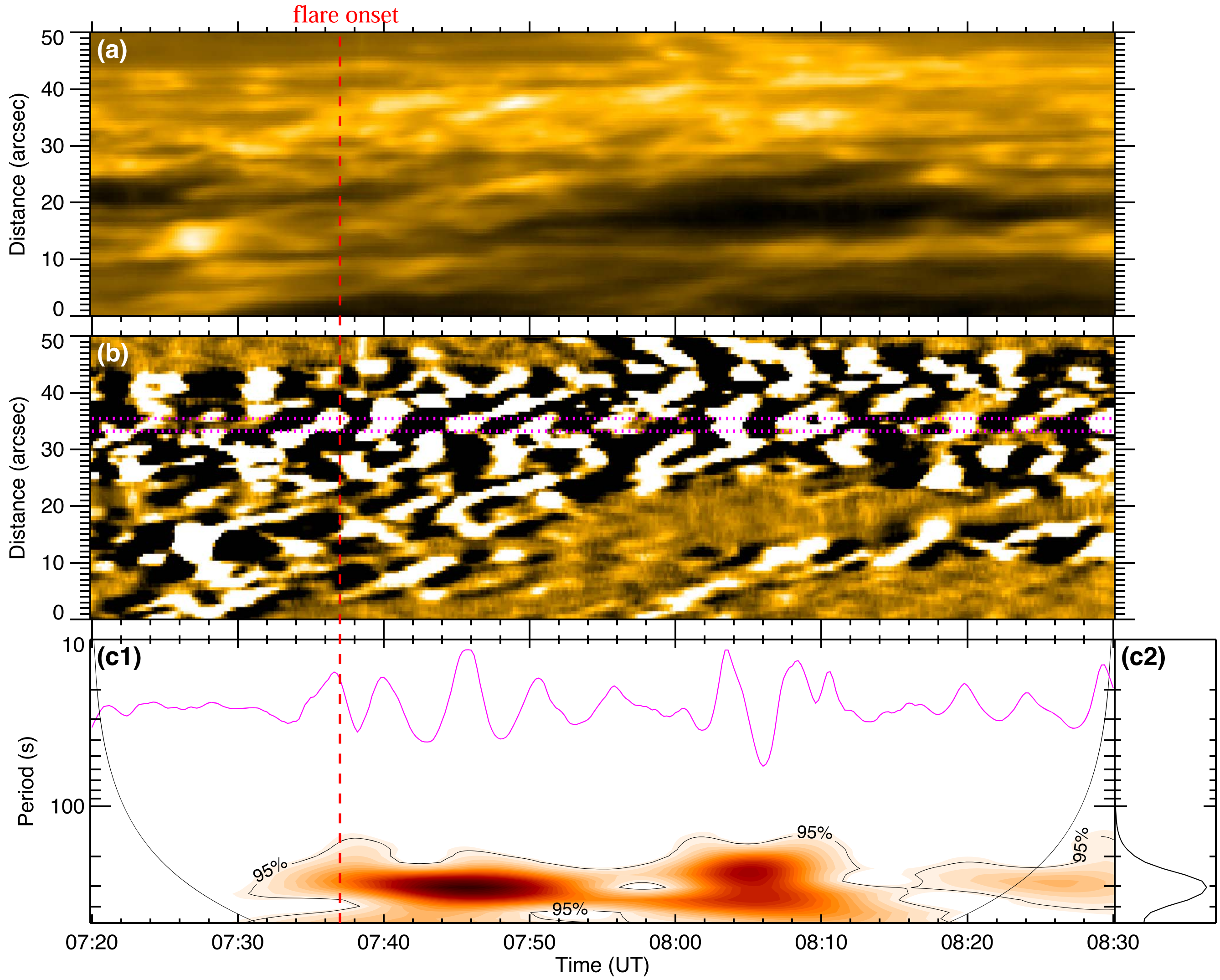

Figure 4. (a) Time–distance diagram of slit-2 in Figure 1(c), and the vertical red dotted line labels the onset of flare. (b) The smooth-subtracted image of the top panel. (c1) The wavelet spectrum of the magenta curve, which represents the rapidly varying components between two horizontal magenta lines in panel (b). (c2) The corresponding global power spectrum.

velocity in the plane-of-the-sky. Next, in Figure 3(b), the fitting results as shown in cyan curves, and their key parameters are listed in Table 1, in which the radius of the cross-section of the loop result from a Gaussian fitting (Petrova et al. 2022). To get the minor radius of loop, we select the column pixels in Figure 3(a), which represent the intensity in the direction of perpendicular to the loop, and a Gaussian profile is used to fit the intensity. Thus, the half width at half maximum (HWHM) of Gaussian fitting is the radius of the loop, which can be calculated from HWHM $= \sqrt{2\ln 2}\,\sigma$.

These oscillations almost have the period of 5 minutes and adjacent loops oscillate in phase. The average displacement amplitude of these oscillations is about 0.55 Mm, which is smaller than the radius of these loops cross-section. Obviously, these oscillations can last for at least two cycles without significant damping, indicating they are decayless. It is interesting that the loop oscillations are independent of the flare eruption. The red dotted line labels the flare starting. Oscillations 1–5 take place at the interval including the flare lifetime from 07:37 UT to 07:44 UT. Their oscillating behaviors do not change as well as no flare eruption. This is because that oscillating loops in Figure 3 are not the flare loops. Figure 1(d) shows the flare loops connected the flare ribbons are bright during the eruption, and they are oblique along the diagonal direction of the AR. We do not find oscillating behaviors in these loops.

Figure 4(a) shows the time–distance diagram of slit-2, and the vertical red dotted line labels the onset of flare. There are

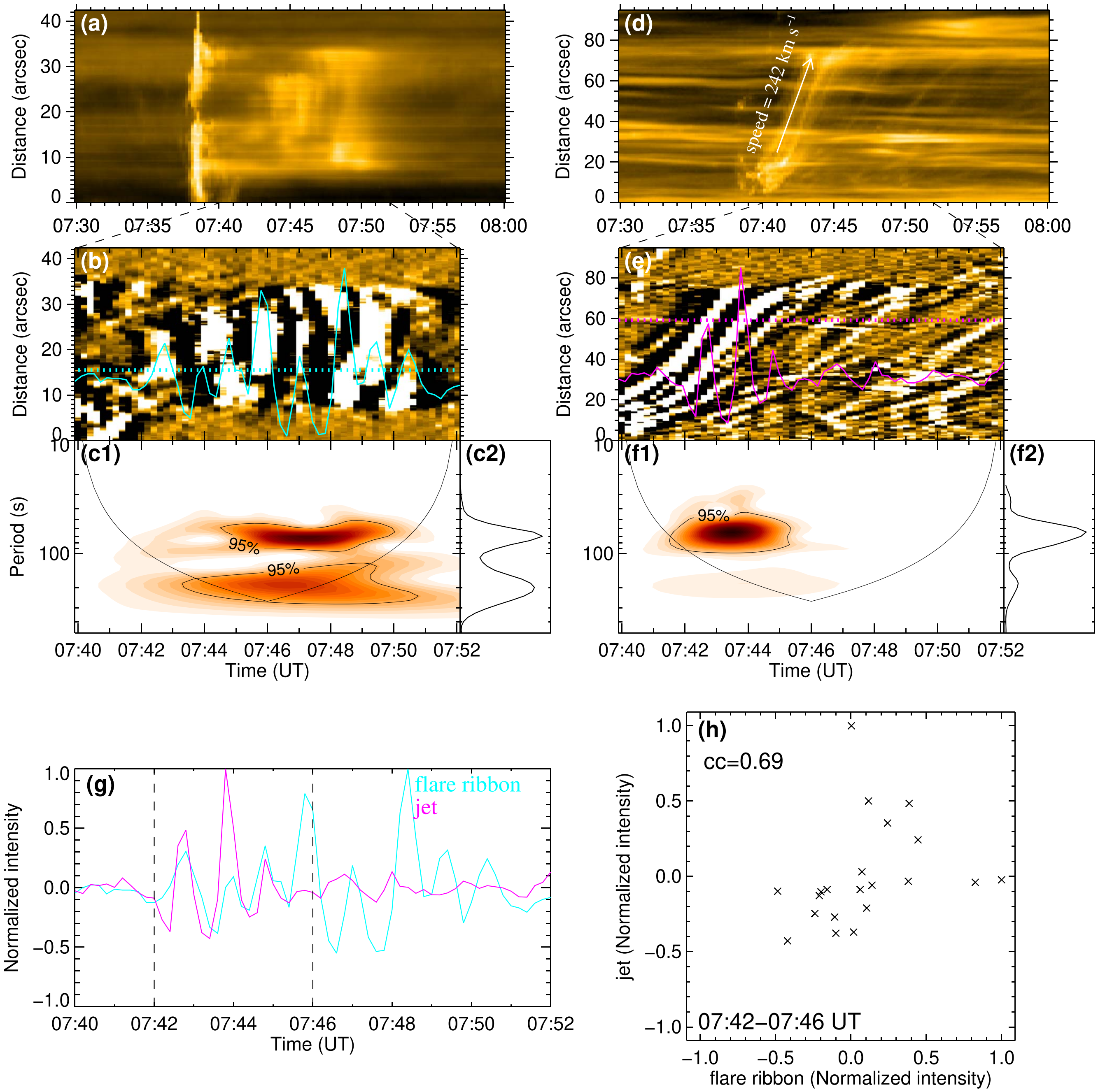

Figure 5. (a) Time–distance diagram of slit-3 in Figure 1(c). (b) The smooth-subtracted image, and the cyan curve represents the rapidly varying component in the position of cyan horizontal line. (c1)–(c2) The wavelet spectrum of the cyan curve and its global power spectrum. (d) Time–distance diagram of slit-4. (e) The smooth-subtracted image, and the magenta curve represents the rapidly varying component in the position of magenta line. (f1)–(f2) The wavelet spectrum of the magenta curve and its global power spectrum. (g) The normalized intensity fluctuations of flare ribbon and jet. (h) The correlation between the intensity fluctuation of flare ribbon and that of jet. The correlation coefficient (cc) is also given.

lots of oscillating loops but they do not display obvious transverse oscillations in the plane-of-the-sky as shown in Figure 3. This is because slit-2 at the loop top is perpendicular to the oscillations. In order to see oscillations clearly, Figure 4(b) gives the smooth-subtracted image of the top panel, i.e., after subtracting the slowly varying component, which is a 300 s running average of original intensity. Therefore, the intensity fluctuations are shown through bright and dark kernels, which represent the enhanced and weakened emission intensity, respectively. These oscillations are the kink modes with vertical polarization (i.e., displace in the loop plane rather than perpendicular to, so they show no obvious displacements in the plane-of-the-sky), which were found to be coupled to the electron density variation (Aschwanden & Schrijver 2011). The rapidly varying component between two horizontal magenta lines is plotted in Figure 4(c1) with the magenta curve, and the corresponding wavelet spectrum is also given, from which we can see the dominant period is around 5 minutes, indicating coronal loops oscillate with the period of 5 minutes. This is consistent with the 5 minutes period obtained from previous decayless kink oscillations.

3.2. Oscillations in Flare Ribbon and Jet

As noted earlier, this flare is a three-ribbon event (see online animation AIA_171.mp4). Figures 1(d) and (e) show that the northeast ribbon is composed of several bright kernels, while the middle and southwest ribbons are not, just bright lines. The AIA animation shows that all ribbons increase their brightness to maximum and then decay accompanying the *GOES* SXR light curve. However, we find the middle and southwest ribbons brightness oscillating. As shown in Figure 1(c), we outline slit-3 along the two ribbons. Here, a constant width of $6''$ (10 pixels) is used for this slit, which is wide enough to cover the ribbon brightness at various times. The two ribbons are along the northeast-southwest direction, thus slit-3 is nearly a straight line. After integrating the brightness along the width of slit, Figure 5(a) displays the time–distance diagram of the two ribbons from 07:30 UT to 08:00 UT at AIA 171 Å. The *Y*-axis is ribbon distance from solar north to south. The middle and southwest ribbons are separated about $3''$ at around $20''$ of the *Y*-axis, and they display their maximum brightness at 07:38:30 UT simultaneously, which is earlier about 90 s than the *GOES* SXR maximum. These pixels around 07:38:30 UT are saturated due to the strong emission at maximum brightness. Figure 5(a) shows some bright stripes periodic appearance, although they are little faint by eyes. Using the same method as Figure 4, but subtract a 72 s running average of original intensity instead of previous 300 s, the smooth-subtracted image of Figure 5(a) is shown in Figure 5(b) from 07:40 UT to 07:52 UT, in which the ribbon intensity oscillations are apparent than in original time–distance image. The cyan curve is overplotted along the dotted line at around $15''$ of the *Y*-axis. It represents the rapidly varying component of the ribbon brightness. Figures 5(c1) and (c2) give the wavelet spectrum and global power of the cyan curve. The result shows that 1 minute is the typical oscillatory period of the middle and southwest ribbons simultaneously.

The AIA animation also displays a jet eject forward the south direction from near the middle ribbon. This jet is intermittent and seems have a periodicity. In order to analyze the period, slit-4 is outlined along the trajectory of jet, as shown in Figure 1(c). The plasma blobs of jet change their direction with time, thus slit-4 is not a straight line but a curve with a width of $3''$ (5 pixels). Figure 5(d) gives the time–distance diagram image from 07:30 UT to 08:00 UT at AIA 171 Å. The *Y*-axis is along the trajectory of jet from solar north to south. The main eruption of jet last for about three minutes, and each ejection is the plasma blob propagating outer. Thus, each ejection appears as an oblique stripe in Figure 5(d). The slope of these stripes is the speed of jet, which is detected as 242 km s^{-1}. Figure 5(e) gives the smooth-subtracted image, and each blob is enhanced and more clearly. The magenta curve is plotted at $59''$ of the *Y*-axis, and several peaks indicating the different plasma blobs. Figures 5(f1) and (f2) give the wavelet spectrum and global power of the magenta curve. Similar to the flare ribbon, the jet have a typical period of 1 minute.

Figures 5(b) and (e) show that the ribbon is oscillating as similar to the jet, i.e., at the same interval between 07:42 UT and 07:46 UT, almost at the same phase. Figure 5(g) plots the light curves of flare ribbon (cyan) and jet (magenta) after subtracting smooth background. Although the peak values of two light curves are different, they are correlated and almost in phase. Figure 5(h) plots the correlation between two curves, the correlation coefficient (cc) of 0.69 further confirms the fact that they are oscillating in phase.

4. Discussion and Conclusions

We study the loop oscillations in AR NOAA 12891 near the solar disk center for more than one hour, in which a C2.0 three-ribbon flare takes place accompanying a periodic jet on 2021 November 2. As usual as other ARs, there are plenty of coronal loops connecting the positive and negative fields. SDO/AIA observation shows that these coronal loops are dynamics, especially, we find some of loops are oscillating with a typical period of 5 minute. It is interesting that not all loops in AR 12891 display the oscillatory behavior, i.e., the loops at the north and south of the AR, as shown in Figure 1(c). These loops are oblique and have an angle to the equator, while the loops between them are oscillating and seem to parallel to the equator.

The AIA observation gives us an opportunity to study the loop oscillation from the loop top and side. In other words, we can present the loop behavior from two views, parallel and perpendicular to the oscillatory direction. Figure 3 gives the loop oscillation from the loop side view. Their oscillating trajectories are outlined and we can conclude the transverse wave mode. The oscillatory amplitude and the period are well detected from the observation. The results show that the loop oscillations are decayless. Figure 4 shows the loop oscillations from the loop top view. In this case, the transverse oscillations display bright and dark kernels, and only the period can be detected from the observation, other parameters such as the amplitude cannot.

Based on the observed 5 minutes oscillations of coronal loops in the present case, we can make some seismological diagnostics to estimate the coronal magnetic field strength (Nakariakov & Ofman 2001; White & Verwichte 2012; Nisticò et al. 2013). These loops oscillations are most likely the standing fundamental kink modes, we can use the relation between kink speed ($C_{\rm k}$) and internal Alfvén speed ($C_{\rm Ai}$), as

$$C_{\rm k} = \frac{2L}{P} = \sqrt{\frac{2}{1+\rho_e/\rho_i}}\,C_{\rm Ai}, \tag{2}$$

where L, P, ρ_e, ρ_i are the length of loop, oscillatory period, external and internal plasma density, respectively. From the AIA images, the radii of these loops are similar, and the value is about 40″, thus the length of loop can be estimated ($L \approx \pi R$). Assuming the ratio of density $\rho_e/\rho_i \approx 0.1$ (Nakariakov & Ofman 2001), and combine the observed typical 5 minutes period, we can obtain $C_{\rm Ai} \approx 466$ km s^{-1}. Then, the magnetic field can be derived from

$$B = C_{\rm Ai}\sqrt{\mu_0 \rho_i} = C_{\rm Ai}\sqrt{\mu_0 n_{\rm i} m_{\rm p} \mu_{\rm c}}, \tag{3}$$

where μ_0, $n_{\rm i}$, $m_{\rm p}$, $\mu_{\rm c}$ are the magnetic permeability in vacuum, internal electron number density, proton mass and the mean molecular weight ($\mu_{\rm c} = 1.27$; Nakariakov & Ofman 2001; White & Verwichte 2012; Nisticò et al. 2013). If assuming the number density $n_{\rm i} = 10^{15}$ m^{-3}, the coronal magnetic field strength $B \approx 7.6$ G, which is similar to the expected value.

There is a C-class three-ribbon flare eruption during the loop oscillating, we find the loop oscillations are independent of the flare eruption. This is because the oscillating loops are not the flare loops, as shown in Figure 1(d). The flare loops are located at the north of the oscillating loops, and they are oblique to the equator. It is still an open question that such loops are not oscillating in the AR.

However, we find that brightening of middle and southwest ribbons of the three-ribbon flare displays the oscillation, and with the typical period of 1 minute. The 1 minute oscillations in solar flare are reported before (Simões et al. 2013; Ning 2017; Shen et al. 2018a; Li et al. 2020, 2021; Li & Chen 2022; Shi et al. 2022). In this event, the accompanying jet also shows the 1 minute period, and the jet eject from the region near the oscillating ribbon. Our analysis indicate that both the jet and ribbon are almost oscillating in phase during the same interval.

Theoretically, the coronal loops display the 5 minutes decayless oscillations, which could be related to the solar global p-mode oscillations. It is reasonable that the p-mode oscillations propagating into the coronal loops from the footpoints (De Moortel et al. 2002; De Pontieu et al. 2005). In this case, all the coronal loops could oscillate with a typical period of 5 minutes. However, we find not all, but some loops display such oscillations. This fact suggests that there is an external driver or transmitter between the coronal loops and the global p-mode oscillations. Besides the possible global p-mode oscillations, small-scale reconnection events at the loop footpoints and upflows might be other reasons to maintain the decayless loop oscillations. However, we did not find related evidence due to the limitation of spatio-resolution and the lack of spectral observation. This needs much more works on both theory and observation to find an answer.

It is obvious that both the flare ribbon and jet display 1 minute periodicity, thus they could come from the same physical process, i.e., periodic magnetic reconnection (McLaughlin et al. 2012; Karampelas et al. 2022a, 2022b) scenario, which can produce the intermittent phenomenon with a periodicity. However, this mechanism seems not suitable here since we did not observe any evidence for supporting this interpretation. Alternatively, since we detected periodic plasmoids along the jet spire, the periodic behavior of the plasmoids and the flare ribbon could be the result of the periodic generation of plasmoids in the reconnection which produced the jet.

Acknowledgments

This research was funded by NSFC under Grant Nos. 12073081, 11973092 and 11790302, as well as CAS Strategic Pioneer Program on Space Science under Grant Nos. XDA15052200 and XDA15320301. D.L. is supported by Surface Project of Jiangsu No. BK20211402. We are grateful to the SDO and *GOES* teams for public access to data. We also thank the referee for providing valuable comments.

ORCID iDs

Fanpeng Shi https://orcid.org/0000-0003-0779-3712
Zongjun Ning https://orcid.org/0000-0002-9893-4711
Dong Li https://orcid.org/0000-0002-4538-9350

References

Afanasyev, A. N., Van Doorsselaere, T., & Nakariakov, V. M. 2020, A&A, 633, L8
Anfinogentov, S. A., Nakariakov, V. M., & Nisticò, G. 2015, A&A, 583, A136
Arregui, I., Oliver, R., & Ballester, J. L. 2018, LRSP, 15, 3
Asai, A., Ishii, T. T., Isobe, H., et al. 2012, ApJL, 745, L18
Aschwanden, M. J., Fletcher, L., Schrijver, C. J., & Alexander, D. 1999, ApJ, 520, 880
Aschwanden, M. J., & Schrijver, C. J. 2011, ApJ, 736, 102
Dai, J., Zhang, Q. M., Su, Y. N., & Ji, H. S. 2021, A&A, 646, A12
De Moortel, I., Ireland, J., Hood, A. W., & Walsh, R. W. 2002, A&A, 387, L13
De Pontieu, B., Erdélyi, R., & De Moortel, I. 2005, ApJL, 624, L61
Gao, Y., Tian, H., Van Doorsselaere, T., & Chen, Y. 2022, ApJ, 930, 55
Hong, Z., Wang, Y., & Ji, H. 2022, ApJ, 928, 153
Karampelas, K., McLaughlin, J. A., Botha, G. J. J., & Régnier, S. 2022a, ApJ, 925, 195
Karampelas, K., McLaughlin, J. A., Botha, G. J. J., & Régnier, S. 2022b, ApJ, 933, 142
Kupriyanova, E., Kolotkov, D., Nakariakov, V., & Kaufman, A. 2020, STP, 6, 3
Lemen, J. R., Title, A. M., Akin, D. J., et al. 2012, SoPh, 275, 17
Li, D., & Chen, W. 2022, ApJL, 931, L28
Li, D., Ge, M., Dominique, M., et al. 2021, ApJ, 921, 179
Li, D., Lu, L., Ning, Z., et al. 2020, ApJ, 893, 7

Li, D., Shen, Y., Ning, Z., Zhang, Q., & Zhou, T. 2018, ApJ, 863, 192
Li, D., Xue, J., Yuan, D., & Ning, Z. 2022, SCPMA, 65, 239611
Lin, Y., Engvold, O., Rouppe van der Voort, L. H. M., & van Noort, M. 2007, SoPh, 246, 65
Liu, R., Liu, C., Xu, Y., et al. 2013, ApJ, 773, 166
Liu, W., Title, A. M., Zhao, J., et al. 2011, ApJL, 736, L13
Luna, M., Knizhnik, K., Muglach, K., et al. 2014, ApJ, 785, 79
Masson, S., Pariat, E., Aulanier, G., & Schrijver, C. J. 2009, ApJ, 700, 559
McLaughlin, J. A., Nakariakov, V. M., Dominique, M., Jelínek, P., & Takasao, S. 2018, SSRv, 214, 45
McLaughlin, J. A., Thurgood, J. O., & MacTaggart, D. 2012, A&A, 548, A98
Miao, Y., Li, D., Yuan, D., et al. 2021, ApJL, 908, L37
Nakariakov, V. M., Anfinogentov, S. A., Antolin, P., et al. 2021, SSRv, 217, 73
Nakariakov, V. M., Anfinogentov, S. A., Nisticò, G., & Lee, D. H. 2016, A&A, 591, L5
Nakariakov, V. M., & Kolotkov, D. Y. 2020, ARA&A, 58, 441
Nakariakov, V. M., & Melnikov, V. F. 2009, SSRv, 149, 119
Nakariakov, V. M., & Ofman, L. 2001, A&A, 372, L53
Nakariakov, V. M., Ofman, L., Deluca, E. E., Roberts, B., & Davila, J. M. 1999, Sci, 285, 862
Ning, Z. 2017, SoPh, 292, 11
Ning, Z., Cao, W., Okamoto, T. J., Ichimoto, K., & Qu, Z. Q. 2009, A&A, 499, 595
Nisticò, G., Nakariakov, V. M., & Verwichte, E. 2013, A&A, 552, A57
O'Dwyer, B., Del Zanna, G., Mason, H. E., Weber, M. A., & Tripathi, D. 2010, A&A, 521, A21
Okamoto, T. J., Nakai, H., Keiyama, A., et al. 2004, ApJ, 608, 1124
Okamoto, T. J., Tsuneta, S., Berger, T. E., et al. 2007, Sci, 318, 1577
Oliver, R., & Ballester, J. L. 2002, SoPh, 206, 45
Pariat, E., Antiochos, S. K., & DeVore, C. R. 2010, ApJ, 714, 1762
Pesnell, W. D., Thompson, B. J., & Chamberlin, P. C. 2012, SoPh, 275, 3
Petrova, E., Magyar, N., Van Doorsselaere, T., & Berghmans, D. 2022, arXiv:2205.05319
Schou, J., Scherrer, P. H., Bush, R. I., et al. 2012, SoPh, 275, 229
Schrijver, C. J., Aschwanden, M. J., & Title, A. M. 2002, SoPh, 206, 69
Shen, Y. 2021, RSPSA, 477, 217
Shen, Y., Ichimoto, K., Ishii, T. T., et al. 2014a, ApJ, 786, 151
Shen, Y., & Liu, Y. 2012, ApJ, 753, 53
Shen, Y., Liu, Y., Song, T., & Tian, Z. 2018a, ApJ, 853, 1
Shen, Y., Liu, Y., Su, J., & Ibrahim, A. 2011, ApJL, 735, L43
Shen, Y., Liu, Y. D., Chen, P. F., & Ichimoto, K. 2014b, ApJ, 795, 130
Shen, Y., Liu, Y. D., Su, J., Qu, Z., & Tian, Z. 2017, ApJ, 851, 67
Shen, Y., Qu, Z., Yuan, D., et al. 2019a, ApJ, 883, 104
Shen, Y., Qu, Z., Zhou, C., et al. 2019b, ApJL, 885, L11
Shen, Y., Song, T., & Liu, Y. 2018b, MNRAS, 477, L6
Shen, Y., Zhou, X., Duan, Y., et al. 2022, SoPh, 297, 20
Shi, F., Li, D., & Ning, Z. 2022, Univ, 8, 104
Simões, P. J. A., Fletcher, L., Hudson, H. S., & Russell, A. J. B. 2013, ApJ, 777, 152
Tian, H., McIntosh, S. W., Wang, T., et al. 2012, ApJ, 759, 144
Toriumi, S., & Wang, H. 2019, LRSP, 16, 3
Van Doorsselaere, T., Kupriyanova, E. G., & Yuan, D. 2016, SoPh, 291, 3143
Wang, H., & Liu, C. 2012, ApJ, 760, 101
White, R. S., & Verwichte, E. 2012, A&A, 537, A49
Zhang, Q. M., Guo, J. H., Tam, K. V., & Xu, A. A. 2020, A&A, 635, A132
Zhang, Q. M., & Ji, H. S. 2014, A&A, 567, A11
Zhang, Q. M., & Ji, H. S. 2018, ApJ, 860, 113
Zhang, Q. M., & Ni, L. 2019, ApJ, 870, 113
Zimovets, I. V., McLaughlin, J. A., Srivastava, A. K., et al. 2021, SSRv, 217, 66
Zimovets, I. V., & Nakariakov, V. M. 2015, A&A, 577, A4